ChemComm

COMMUNICATION

View Article Online
View Journal | View Issue

Cite this: *Chem. Commun.*, 2016, 52, 1226

Received 10th October 2015,
Accepted 17th November 2015

DOI: 10.1039/c5cc08418k

www.rsc.org/chemcomm

Platinum nanoparticles encapsulated metal–organic frameworks for the electrochemical detection of telomerase activity†

Pinghua Ling, Jianping Lei,* Li Jia and Huangxian Ju

A simple and rapid electrochemical sensor is constructed for the detection of telomerase activity based on the electrocatalysis of platinum nanoparticle (Pt NP) encapsulated metal–organic frameworks (MOFs), which are synthesized by one-pot encapsulation of Pt NPs into prototypal MOFs, UiO-66-NH_2. Integrating with the efficient electrocatalysis of Pt@MOFs towards $NaBH_4$ oxidation, this biosensor shows the wide dynamic correlation of telomerase activity from 5×10^2 to 10^7 HeLa cells mL^{-1} and the telomerase activity in a single HeLa cell was calculated to be 2.0×10^{-11} IU, providing a powerful platform for detecting telomerase activity.

Telomerase consisting of $(TTAGGG)_n$ repeats[1] has been regarded as both a cancer marker for early cancer diagnosis and a therapeutic target owing to its strong association with cell immortalization and tumorigenesis.[2] In most human somatic cells, the telomerase activity is highly depressed but telomerase has been observed to be over-expressed to over 85% in human tumors.[3] Numerous methods have been developed for the detection of the telomerase activity, such as polymerase chain reaction,[4] electrochemiluminescence,[5] fluorescence,[6] chemiluminescence[7] and electrochemical methods.[8] Most of these developed probes provide a useful platform for telomerase assay. For example, a Cy5-tagged molecular beacon functionalized gold nanoparticle probe was designed for *in situ* fluorescence imaging and detection of cytoplasmic telomerase activity.[9] An electrochemical biosensor with ferrocene as the electroactive reporter was developed to detect telomerase activity *via* DNA structure-switching.[10] The signal readout of above methods always originates from the direct electrochemical signal or fluorescence "off"–"on" transduction. To trace the telomerase activity, an amplified signal, especially for a catalytic signal, is highly desirable to design a facile and sensitive strategy.

Noble-metal nanoparticles (NPs), such as Au, Pd, and Pt, have been widely studied in heterogeneous catalysis owing to their unique structures. However, these free noble-metal NPs are easy to be aggregated. In order to overcome the drawback of NPs,[11] the conventional method is to coat noble-metal NPs with either organic or inorganic shells such as silica,[12] zeolites,[13] and carbon.[14] Recently, metal–organic frameworks (MOFs), a new class of porous crystalline materials synthesized from metal ions/clusters and organic ligands,[15] have shown many applications in gas storage and separations,[16] sensing,[17] and drug delivery[18] owing to their high surface areas, well-defined porosities, and chemical tenability. In particular, MOFs as unique host matrices can offer a platform for the incorporation of metal nanoparticles to generate nanoparticle/MOF composites,[19] which not only makes the metal NPs well-dispersed but also guarantees that the MOF pores are accessible for both reactant and product. There are two strategies for the preparation of nanoparticle/MOF composites including encapsulating pre-synthesized nanoparticles in MOFs[20] or using MOFs as templates to generate nanoparticles within their cavities.[21] In the former, the spatial distribution of pre-synthesized nanoparticles embedded in the MOFs is hardly controlled. However, in the latter, it possesses inherent limitations such as aggregation of NPs on the external surface, the poor control of NP size, and the potential damage of the MOF structures during the post-reduction process of NPs. In addition, a one-step encapsulation of caffeine as a model drug in MOFs was demonstrated for high guest loading and controlled release.[22] In this work, we develop a one-pot strategy for the preparation of Pt NPs-encapsulated MOFs as an electrocatalytic tracer for sensing telomerase activity.

Pt NP-based nanomaterials with highly efficient catalysts towards oxygen or 4-nitrophenol reduction have been utilized in bioanalysis.[23,24] In particular, the electrocatalysis of Pt NPs towards $NaBH_4$ oxidation is multi-electron (maximum $8e^-$). Thus, the electrochemical signal produced in the process is much higher than that from the electrochemical reaction involving one-electron or two-electron oxidation. In view of the structural diversity and tenability of MOFs, we synthesized the Pt NP and MOF composite (Pt@UiO-66-NH_2) *via* one-step, and sequentially immobilized with capture DNA (cDNA) as a signal probe. Coupling with multi-electron

State Key Laboratory of Analytical Chemistry for Life Science, School of Chemistry and Chemical Engineering, Nanjing University, Nanjing 210093, P. R. China. E-mail: jpl@nju.edu.cn; Fax: +86 25 83593593; Tel: +86 25 83593593

† Electronic supplementary information (ESI) available: Experimental details and additional figures. See DOI: 10.1039/c5cc08418k

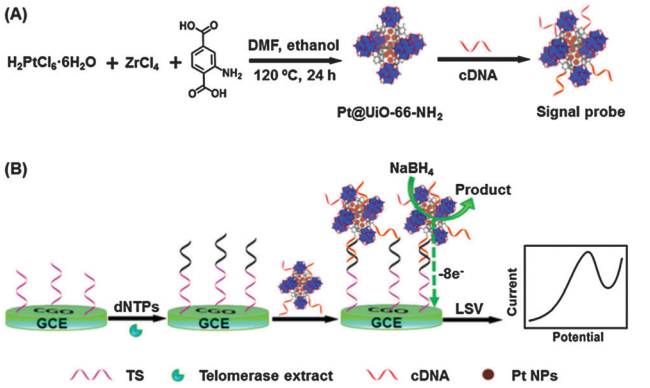

Scheme 1 Schematic representation of (A) Pt@UiO-66-NH_2 preparation and (B) sensing principle for the electrochemical detection of telomerase activity.

electrocatalysis of Pt@UiO-66-NH_2 towards $NaBH_4$ oxidation, a signal-on electrochemical method was designed to detect telomerase activity in cancer cells (Scheme 1). A telomerase primer (TS), which could be extended in the presence of telomerase and dNTPs, was attached onto a glassy carbon electrode (GCE). After the telomerase primer was extended, the Pt@UiO-66-NH_2-cDNA probe could form a hybrid with the extended part on the sensor surface, resulting in a significantly amplified electrocatalytic current towards $NaBH_4$ oxidation. This simple and rapid approach can detect the telomerase activity of HeLa extract in a wide range with a detection limit of 100 HeLa cells mL^{-1}, and the telomerase activity in a single HeLa cell was also calculated. The Pt@MOF offers an excellent signal transduction platform for the detection of telomerase activity, and could be integrated with other recognition elements to broaden its applications in bioassay.

UiO-66-NH_2 and Pt@UiO-66-NH_2 were synthesized using 2-aminoterephthalic acid (NH_2–H_2BDC) as the linker and Zr as the node *via* a solvothermal reaction. The morphology and structure of UiO-66-NH_2 and Pt@UiO-66-NH_2 nanocomposites are firstly investigated using different characterization techniques. The scanning electron microscopy (SEM) images of UiO-66-NH_2 and Pt@UiO-66-NH_2 showed that both crystal structures have octahedral geometry (Fig. 1A and B), which indicates that the Pt NPs did not affect the octahemioctahedral crystal structure. No particles were observed on the surface, suggesting that the formed Pt NPs are well dispersed inside the cavities of the MOFs. The transmission electron microscopy (TEM) images of UiO-66-NH_2 and Pt@UiO-66-NH_2 (Fig. 1C and D) exhibited intact crystal morphology with 100 nm. This is accordance with the results of dynamic light scattering (Fig. S1, ESI†). Notably, Pt NPs were homogeneously distributed inside the UiO-66-NH_2 frameworks with a diameter of ~1.0 nm. During the synthesis of Pt@UiO-66-NH_2, DMF is utilized as both the solvent in NH_2–H_2BDC solution to directly determine the construction of UiO-66-NH_2 and the reducing agent for the effective formation of Pt NPs.[25]

The N_2 adsorption–desorption isotherm profiles and pore size distribution of UiO-66-NH_2 and Pt@UiO-66-NH_2 are shown in Fig. 2A and B. Both adsorption–desorption isotherms show a type I shape, a typical characteristic of microporous materials. This is consistent with the results of pore size distribution (≤2.0 nm).

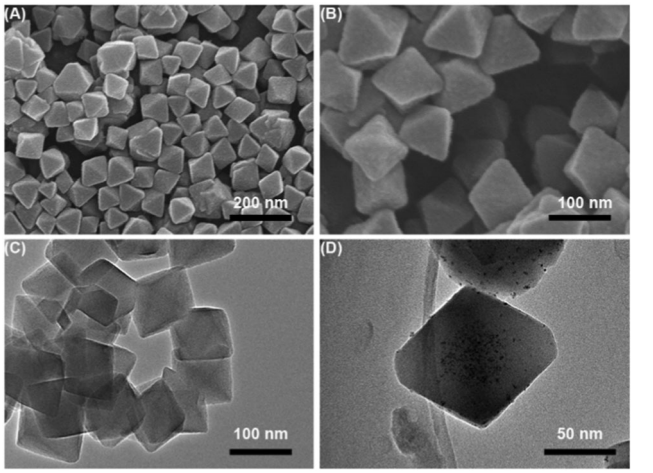

Fig. 1 SEM (A and B) and TEM (C and D) images of (A and C) UiO-66-NH_2 and (B and D) Pt@UiO-66-NH_2.

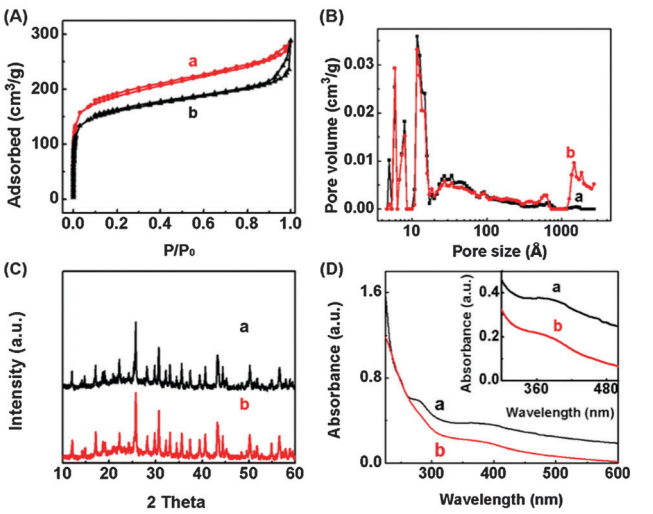

Fig. 2 (A) Nitrogen adsorption–desorption isotherm at 77 K, (B) DFT pore size distribution with N_2 at 77 K, and (C) powder XRD patterns of UiO-66-NH_2 (a) and Pt@UiO-66-NH_2 (b). (D) UV-vis absorption spectra of Pt@UiO-66-NH_2-cDNA (a) and Pt@UiO-66-NH_2 (b).

The Brunauer–Emmett–Teller (BET) surface area and micropore volume of UiO-66-NH_2 were calculated to be 1128 $m^2\ g^{-1}$ and 0.44 $cm^3\ g^{-1}$, respectively. The BET surface area and pore volume of Pt@UiO-66-NH_2 showed a slight decrease (936 $m^2\ g^{-1}$ and 0.36 $cm^3\ g^{-1}$) compared with intrinsic UiO-66-NH_2, respectively, mainly due to the occupation of the cavities of the UiO-66-NH_2 framework by Pt NPs. X-ray photoelectron spectroscopy (XPS) was used to investigate the surface composition of Pt@UiO-66-NH_2 composites (Fig. S2, ESI†). Based on the XPS results, the Pt weight concentration was estimated to be 6.7% in the Pt@UiO-66-NH_2 composite.

The crystal structure and porosity of UiO-66-NH_2 and Pt@UiO-66-NH_2 composites were further characterized by X-ray diffraction (XRD). The XRD curves show the peaks at 14.48, 17.08, 19.16, 22.38, 25.18, and 30.88 degrees, which can be indexed to (222), (400), (420), (511), (600), and (640) of the octahedral geometry (JCPDF card number: 36-1452), indicating the octahemioctahedral

crystal structure of the MOF materials.[19b] Compared to the XRD spectrum of intrinsic UiO-66-NH_2 (Fig. 2C, curve a), no significant loss of crystallinity could be detected in the XRD pattern (Fig. 2C, curve b) after loading with Pt NPs, which is consistent with the results of thermogravimetric analysis shown in Fig. S3 (ESI†). Furthermore, the absence of XRD peaks from Pt nanocrystals could be presumably attributed to the low NP concentration as well as the small size of encapsulated Pt particles in the UiO-66-NH_2 framework.

In the fingerprint region of the IR spectra (Fig. S4, ESI†), the peaks at 3507 cm^{-1}, 3384 cm^{-1}, 1500 cm^{-1} and 1250 cm^{-1} were assigned to $\nu_{asym}(-NH_2)$, $\nu_{sym}(-NH_2)$, $\delta(-NH_2)$, and $\nu(C-N)$,[26] identifying that the UiO-66-NH_2 was functionalized with the $-NH_2$ group. In order to investigate the fabrication process of Pt@UiO-66-NH_2-cDNA, UV-vis absorption spectrometry was used (Fig. 2D). This showed that there was a new absorption peak at 278 nm (Fig. 2D, curve a) compared with pure UiO-66-NH_2 (Fig. 2D, curve b), suggesting that DNA could be bound to the Pt@UiO-66-NH_2 surface.

The electrocatalytic activity of different electrodes towards $NaBH_4$ oxidation was measured in 0.1 M pH 11.0 H_3BO_3–NaOH buffer with cyclic voltammograms (CVs). At the bare GCE and UiO-66-NH_2/GCE, there are no obvious signals in response to $NaBH_4$ in the examined potential range from −0.4 V to 0.6 V (Fig. 3A, curve a and curve b). However, there appeared two typical oxidation peaks at around 0.08 V and −0.17 V corresponding to the oxidation of $NaBH_4$ at the Pt@UiO-66-NH_2/GCE and Pt/GCE electrodes (Fig. 3A, curve c and d). Because $NaBH_4$ undergoes multi-electron (maximum $8e^-$) oxidation on Pt NPs,[27] the current signal could be much higher than those from the electrochemical reactions involving one-electron or two-electron oxidation.[28] Comparing with Pt/GCE, Pt@UiO-66-NH_2/GCE showed a large peak current, which confirmed that the MOFs are an excellent support to load the Pt NPs for electrocatalysis.

The feasibility of the sensor was investigated by conducting linear sweep voltammetry (LSV) in response to $NaBH_4$ (Fig. 3B). When the TS modified GCE incubated with PBS (Fig. 3B, curve a) or heat-treated cell extract in the presence of dNTPs (Fig. 3B, curve c), the small peak current was observed due to the nonspecific adsorption between the UiO-66-NH_2 and the electrode surface. After treatment with the telomerase extract, the TS on the electrode should be extended, and then hybridized with Pt@UiO-66-NH_2-cDNA. Thus, the Pt@UiO-66-NH_2 was introduced onto the GCE surface to catalyze $NaBH_4$ oxidation for a detectable electrochemical signal (Fig. 3B, curve b).

Next, gel electrophoresis was employed to verify the feasibility of this method (Fig. S5, ESI†). To ensure high hybridization efficiency and sensitivity, the TS density should be optimized (Fig. S6, ESI†). When the primer concentration increased, the current reached a maximum at 0.5 μM and then decreased, which was attributed to the reason that increased TS on the electrode surface could hinder the extension of telomerase. The effect of the incubation time and the hybridization time on the electrochemical response is also optimized (Fig. S7A and B, ESI†). The current signal increased gradually up to 90 min and approached a platform (Fig. S7A, ESI†). Therefore, 90 min was selected as the optimal incubation time for the telomerase extension reaction. After TS extension, the Pt@UiO-66-NH_2-cDNA probe would hybridize with the telomere repeats $(TTAGGG)_n$. The hybridization time between Pt@UiO-66-NH_2-cDNA and $(TTAGGG)_n$ is an important parameter that influences the signal. When the hybridization time was more than 90 min, the current signal increased and reached a plateau (Fig. S7B, ESI†). Thus, 90 min was selected as the hybridization time between Pt@UiO-66-NH_2-cDNA and $(TTAGGG)_n$ in the experiments.

The telomerase activity of cell extract was subsequently evaluated by using telomerase extracts from various concentrations of HeLa cells with LSV measurements under the optimal experimental conditions. The dynamic correlation between LSV peak current and telomerase activity demonstrates that the electrochemical signal increased with the increase of concentrations of HeLa cells ranging from 5×10^2 to 1×10^7 HeLa cells mL^{-1} (Fig. 4). The higher the concentration of HeLa cells, the more Pt@UiO-66-NH_2-cDNA was obtained on the electrode surface, resulting in the enhanced catalytic current of Pt@UiO-66-NH_2 towards $NaBH_4$ oxidation. The inset of Fig. 4B shows that the signal from 500 cells could be easily distinguished in the background (Fig. 3B, curve a). The method demonstrates good sensitivity with a detection limit of 100 HeLa cells mL^{-1} as calculated in terms of the rule of 3 times the standard deviation over the blank response. This result was comparable with the sensors reported by other groups.[7,8b]

Additionally, the present strategy possessed excellent repeatability with the obtained the RSD of 3.8%, 4.0% and 4.6% in three repetitive assays of 500, 5000 and 10 000 HeLa cells. The reproducibility of the sensor was also studied, ten independently

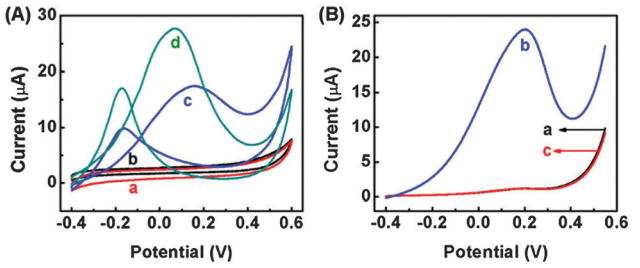

Fig. 3 (A) CVs of bare GCE (a), UiO-66-NH_2/GCE (b), Pt/GCE (c) and Pt@UiO-66-NH_2/GCE (d). (B) LSV responses of TS modified GCE incubated for 90 min in PBS + dNTPs (a), the extract + dNTPs (b) and the heated extract + dNTPs (c). The detection solution is in 0.1 M pH 11.0 H_3BO_3–NaOH buffer containing 5 mM $NaBH_4$. Scan rate: 50 mV s^{-1}.

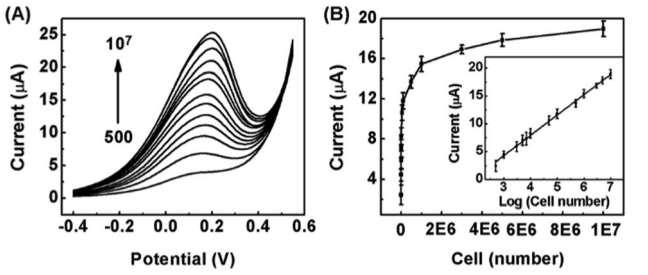

Fig. 4 LSV signals of a range of HeLa cell numbers (from bottom to top): 5×10^2, 10^3, 3×10^3, 5×10^3, 7×10^3, 10^4, 5×10^4, 10^5, 5×10^5, 10^6, 3×10^6, 5×10^6 and 10^7 cells mL^{-1}. (B) The plot of LSV peak currents *vs.* HeLa cell concentrations. Inset shows the corresponding LSV peak currents *vs.* the logarithm of HeLa cell concentrations.

prepared electrodes were used with the RSD of 4.5%. When not in use, it was stored at 4 °C. After 2 weeks, the biosensor still retained 85% of the initial value. Therefore, the results indicated that the developed sensor had excellent repeatability and fabrication reproducibility, and acceptable stability. To detect the telomerase activity in each HeLa cell, the standard curve was obtained by using various concentrations of telomerase (10 μL) under optimal experimental conditions at the TS modified GCE (Fig. S8, ESI†). The telomerase activity was calculated to be 2.0×10^{-11} IU in each HeLa cell, which was slightly less than that of the efficient Au NP probe-based fluorescence resonance energy transfer system (2.9×10^{-11} IU).[9]

To demonstrate the reliability of this method for telomerase detection, other cancer cell lines such as U87, CEM, HEpG2 and MCF-7 cell lines were tested (Fig. S9, ESI†). As expected, all of these cell lines showed positive telomerase activity, except for the heated HeLa cell sample, which is due to the lack of telomerase activity after heating, so it showed a weak background signal. According to the peak current, the telomerase activity of HeLa was higher than that of MCF-7, U87, CEM and HEpG2. These results were consistent with the previous reports that the telomerase could be detected in nearly 85% of human cancer cells, indicating the reliability of our method.

In summary, this work successfully developed a one-pot strategy to prepare Pt NPs-encapsulated MOFs as an electrocatalytic tracer for the rapid and sensitive electrochemical detection of telomerase activity. Owing to the well-defined porosities and chemical tenability of MOFs, the Pt NPs were homogeneously distributed inside the MOF frameworks with a diameter of *ca.* 1.0 nm. The resulting Pt@UiO-66-NH_2 composite demonstrated high electrocatalysis for $NaBH_4$ oxidation *via* multi-electron (maximum $8e^-$) transfer in alkaline solution. On the basis of the high catalytic performance of Pt@UiO-66-NH_2, the designed method can measure the telomerase activity with high sensitivity down to 100 cell mL^{-1} and a wide dynamic range. More significantly, this approach achieved the detection of the telomerase activity in a single cell. Furthermore, the proposed method is more convenient without the need for any additional separation steps. The advantages of the biosensor were also identified by analyzing various other cell lines of telomerase activity. The Pt@MOFs not only offer an excellent platform for elucidating the biofunctionality of telomerase but also easily integrate other signal amplifications for the trace detection of a wide range of the analysts.

This research was supported by the National Natural Science Foundation of China (21375060, 21135002, 21121091) and Priority development areas of the National Research Foundation for the Doctoral Program of Higher Education of China (20130091130005).

Notes and references

1 (*a*) E. H. Blackburn, *Nature*, 1991, **350**, 569–573; (*b*) S. B. Cohen, M. E. Graham, G. O. Lovrecz, N. Bache, P. J. Robinson and R. R. Reddel, *Science*, 2007, **315**, 1850–1853; (*c*) F. Rodier and J. Campisi, *J. Cell Biol.*, 2011, **192**, 547–556.
2 J. W. Shay and W. E. Wright, *Cancer Cell*, 2002, **2**, 257–265.
3 (*a*) K. Masutomi, E. Y. Yu, S. Khurts, I. Ben-Porath, J. L. Currier, G. B. Metz, M. W. Brooks, S. Kaneko, S. Murakami, J. A. DeCaprio, R. A. Weinberg, S. A. Stewart and W. C. Hahn, *Cell*, 2003, **114**, 241–253; (*b*) E. Kavaler, J. Landman, Y. Chang, M. J. Droller and B. C. S. Liu, *Cancer*, 1998, **82**, 708–714.
4 Y. Xiao, K. Y. Dane, T. Uzawa, A. Csordas, J. R. Qian, H. T. Soh, P. S. Daugherty, E. T. Lagally, A. J. Heeger and K. W. Plaxco, *J. Am. Chem. Soc.*, 2010, **132**, 15299–15307.
5 (*a*) L. Wu, J. S. Wang, L. Y. Feng, J. S. Ren, W. L. Wei and X. G. Qu, *Adv. Mater.*, 2012, **24**, 2447–2452; (*b*) H. R. Zhang, M. S. Wu, J. J. Xu and H. Y. Chen, *Anal. Chem.*, 2014, **86**, 3834–3840.
6 (*a*) H. B. Wang, S. Wu, X. Chu and R. Q. Yu, *Chem. Commun.*, 2012, **48**, 5916–5918; (*b*) C. F. Ding, X. L. Li, Y. Ge and S. S. Zhang, *Anal. Chem.*, 2010, **82**, 2850–2855.
7 Y. Li, X. Li, X. T. Ji and X. M. Li, *Biosens. Bioelectron.*, 2011, **26**, 4095–4098.
8 (*a*) Y. Li, Y. L. Wen, L. L. Wang, W. Liang, L. Xu, S. Z. Ren, Z. Y. Zou, X. L. Zuo, C. H. Fan, Q. Huang, G. Liu and N. Q. Jia, *Biosens. Bioelectron.*, 2015, **67**, 364–369; (*b*) W. Q. Yang, X. Zhu, Q. D. Liu, Z. Y. Lin, B. Qiu and G. N. Chen, *Chem. Commun.*, 2011, **47**, 3129–3131.
9 R. C. Qian, L. Ding, L. W. Yan, M. F. Lin and H. X. Ju, *Anal. Chem.*, 2014, **86**, 8642–8648.
10 Z. Yi, H. B. Wang, K. Chen, Q. Gao, H. Tang, R. Q. Yu and X. Chu, *Biosens. Bioelectron.*, 2014, **53**, 310–315.
11 C. B. Gao, Q. Zhang, Z. D. Lu and Y. D. Yin, *J. Am. Chem. Soc.*, 2011, **133**, 19706–19709.
12 J. Wei, H. Wang, Y. H. Deng, Z. K. Sun, L. Shi, B. Tu, M. Luqman and D. Y. Zhao, *J. Am. Chem. Soc.*, 2011, **133**, 20369–20377.
13 Y. S. Tao, H. Kanoh, L. Abrams and K. Kaneko, *Chem. Rev.*, 2006, **106**, 896–910.
14 (*a*) Y. Wan, H. F. Yang and D. Y. Zhao, *Acc. Chem. Res.*, 2006, **39**, 423–432; (*b*) T. Harada, S. Ikeda, Y. H. Ng, T. Sakata, H. Mori, T. Torimoto and M. Matsumura, *Adv. Funct. Mater.*, 2008, **18**, 2190–2196.
15 O. K. Farha and J. T. Hupp, *Acc. Chem. Res.*, 2010, **43**, 1166–1175.
16 (*a*) D. X. Xue, A. J. Cairns, Y. Belmabkhout, L. Wojtas, Y. L. Liu, M. H. Alkordi and M. Eddaoudi, *J. Am. Chem. Soc.*, 2013, **135**, 7660–7667; (*b*) S. Keskin, T. M. van Heest and D. S. Sholl, *ChemSusChem*, 2010, **3**, 879–891.
17 (*a*) L. E. Kreno, K. Leong, O. K. Farha, M. Allendorf, R. P. Van Duyne and J. T. Hupp, *Chem. Rev.*, 2012, **112**, 1105–1125; (*b*) C. B. He, K. D. Lu and W. B. Lin, *J. Am. Chem. Soc.*, 2014, **136**, 12253–12256.
18 C. B. He, K. D. Lu, D. M. Liu and W. B. Lin, *J. Am. Chem. Soc.*, 2014, **136**, 5181–5184.
19 (*a*) M. T. Zhao, K. Deng, L. C. He, Y. Liu, G. D. Li, H. J. Zhao and Z. Y. Tang, *J. Am. Chem. Soc.*, 2014, **136**, 1738–1741; (*b*) W. N. Zhang, G. Lu, C. L. Cui, Y. Y. Liu, S. Z. Li, W. J. Yan, C. Xing, Y. R. Chi, Y. H. Yang and F. W. Huo, *Adv. Mater.*, 2014, **26**, 4056–4060.
20 (*a*) P. Falcaro, A. J. Hill, K. M. Nairn, J. Jasieniak, J. I. Mardel, T. J. Bastow, S. C. Mayo, M. Gimona, D. Gomez, H. J. Whitfield, R. Ricco, A. Patelli, B. Marmiroli, H. Amenitsch, T. Colson, L. Villanova and D. Buso, *Nat. Commun.*, 2011, **2**, 237; (*b*) M. R. Lohe, K. Gedrich, T. Freudenberg, E. Kockrick, T. Dellmann and S. Kaskel, *Chem. Commun.*, 2011, **47**, 3075–3077.
21 (*a*) D. Esken, S. Turner, O. I. Lebedev, G. V. Tendeloo and R. A. Fischer, *Chem. Mater.*, 2010, **22**, 6393–6401; (*b*) H. L. Jiang and Q. Xu, *Chem. Commun.*, 2011, **47**, 3351–3370; (*c*) X. J. Gu, Z. H. Lu, H. L. Jiang, T. Akita and Q. Xu, *J. Am. Chem. Soc.*, 2011, **133**, 11822–11825.
22 (*a*) N. Liédana, A. Galve, C. Rubio, C. Téllez and J. Coronas, *ACS Appl. Mater. Interfaces*, 2012, **4**, 5016–5021; (*b*) N. Liédana, P. Lozano, A. Galve, C. Télleza and J. Coronas, *J. Mater. Chem. B*, 2014, **2**, 1144–1151.
23 C. Z. Zhu, G. H. Yang, H. Li, D. Du and Y. H. Lin, *Anal. Chem.*, 2015, **87**, 230–249.
24 (*a*) S. F. Fu, G. H. Yang, Y. Z. Zhou, H. B. Pan, C. M. Wai, D. Du and Y. H. Lin, *RSC Adv.*, 2015, **5**, 32685–32689; (*b*) J. Tang, J. Zhou, Q. F. Li, D. P. Tang, G. N. Chen and H. H. Yang, *Chem. Commun.*, 2013, **49**, 1530–1532.
25 (*a*) H. Yamamoto, H. Yano, H. Kouchi, Y. Obora, R. Arakawa and H. Kawasaki, *Nanoscale*, 2012, **4**, 4148–4154; (*b*) L. Rodríguez-Lorenzo, R. de la Rica, R. A. Álvarez-Puebla, L. M. Liz-Marzán and M. M. Stevens, *Nat. Mater.*, 2012, **11**, 604–607.
26 M. Kandiah, M. H. Nilsen, S. Usseglio, S. Jakobsen, U. Olsbye, M. Tilset, C. Larabi, E. A. Quadrelli, F. Bonino and K. P. Lillerud, *Chem. Mater.*, 2010, **22**, 6632–6640.
27 C. P. de Leon, F. C. Walsh, D. Pletcher, D. J. Browning and J. B. Lakeman, *J. Power Sources*, 2006, **155**, 172–181.
28 J. Das, H. Kim, K. Jo, K. H. Park, S. Y. Jon, K. Lee and H. Yang, *Chem. Commun.*, 2009, 6394–6396.